Supplementary Material

Regional and weather-type modulation of global warming–driven intensification of Italian precipitation extremes from multi-year storyline simulations

Marco Burderi[1], Salvatore Pascale[1], Cristina Iacomino[3, 4, 1], Federico Grazzini[2,5], Matteo Nurisso[6, 7], Amal John[8], Sebastian Beyer[8], Giuseppe Zappa[2]

[1]University of Bologna, Department of Physics and Astronomy (DIFA), Bologna, Italy

[2]National Research Council of Italy, Institute of Atmospheric Sciences and Climate (ISAC), Bologna, Italy

[3]Fondazione Bruno Kessler, Data Science for Industry and Physics (DSIP), Trento, Italy

[4]University of Trento, Department of Civil, Environmental and Mechanical Engineering (DICAM), Trento, Italy

[5]Struttura IdroMeteoClima, ARPAE, Bologna, Italy

[6]National Research Council of Italy, Institute of Atmospheric Sciences and Climate (ISAC), Torino, Italy

[7]Department of Environment, Land and Infrastructure Engineering (DIATI) Politecnico di Torino, Torino, Italy

[8]Alfred-Wegener-Institut, Helmholtz-Zentrum für Polar und Meeresforschung (AWI), Bremerhaven, Germany

July 2, 2026

Corresponding author: Marco Burderi
email: marco.burderi@studio.unibo.it marco.burd@gmail.com

Supplementary text

S1. IFS-FESOM Model and Nudging Details

The IFS–FESOM model couples ECMWF's Integrated Forecasting System (IFS) for atmosphere, land, and waves with the Finite-volumE Sea-ice Ocean Model (FESOM2), including fully coupled atmosphere–ocean–sea-ice and land-surface interactions. The atmosphere is simulated at TCo1279 triangular spectral truncation (∼9 km horizontal spacing) with 137 vertical levels, using a semi-Lagrangian, semi-implicit, hydrostatic dynamical core. The ocean component employs an unstructured triangular mesh with NG5 variable resolution (12 km at the equator, 4.5 km in dynamically active regions) and 70 vertical layers, designed for eddy-rich simulations.

Spectral nudging is applied to the spherical harmonic components up to T60 truncation (corresponding to resolved scales of approximately 1,000 km near the equator and proportionally smaller toward higher latitudes) for vorticity and divergence fields in the mid- and upper troposphere (between 700 and 100 hPa). This configuration constrains the large-scale circulation while allowing mesoscale processes, the planetary boundary layer, and orographic convection to freely evolve. Further technical details of the nudging implementation are provided in John et al. (2026). Full model references: Danilov et al. (2017); Scholz et al. (2019, 2022); Temperton et al. (2001); Hortal (2002); Diamantakis and Váňa (2022).

S2. Spectral Nudging Implementation

Spectral nudging constrains only large-scale dynamical atmospheric variables in the spectral domain, so that their tendency equations become:

$$\frac{\partial X_n^m(\eta, t)}{\partial t} = F_n^m(\eta, t) + G_n^m(\eta)\Big[X_n^{m\,(reanalysis)}(\eta, t) - X_n^m(\eta, t)\Big], \tag{1}$$

where m, n are zonal and total wavenumbers, X_n^m are spectral coefficients, F_n^m the model forcing, and $G_n^m(\eta)$ the nudging strength.

The key aspects of the implemented nudging scheme are the following:

- Variables nudged: vorticity and divergence only.
- Spectral truncation: nudging is only applied up to spherical harmonic T60 ($\lambda \gtrsim 1000$ km), allowing mesoscale features to evolve freely.
- Vertical extent of nudging: 700–100 hPa. A smooth sigmoid weighting reduces nudging near the upper and lower boundaries.
- E-folding time: $\tau = 1\,\text{h}$, providing rapid adjustment while preserving small-scale variability.

Sensitivity tests showed minimal influence when nudging included the stratosphere or planetary boundary layer (John et al., 2026).

S3. Ocean Spin-Up and Initialization

Control (Cont) and *Historical* (Hist) simulations: 5-year ocean-only spin-up (1945–1949 and 2012–2016 respectively), atmospheric initial conditions from ERA5 (2017-01-01). Residual inconsistencies affect deep-ocean states, but fast-atmosphere and near-surface variables converge rapidly, justifying the use of 2017–2024 period for precipitation analyses.

S4. Weather-Type Classification (SOM)

The large-scale circulation associated with extreme precipitation events (EPEs) is characterised using the weather-type (WT) classification developed by Iacomino et al. (2025), based on Self-Organising Maps (SOMs).

- **Input fields**: Daily mean 500 hPa geopotential height (Z500) and mean sea-level pressure (MSLP) from ERA5 reanalysis, corresponding to the EPEs identified in the CERRA-based catalogue.
- **Training period**: November 1984 to October 2024, ensuring a consistent representation of circulation variability over the full observational record.

- **SOM configuration**: A two-dimensional 3x2 SOM grid is used to map high-dimensional atmospheric fields onto a reduced set of representative circulation patterns while preserving their topological relationships. Each node represents a distinct large-scale circulation regime.

- **Event assignment**: Each EPE is assigned to the closest SOM node based on similarity in the input fields, thereby grouping events into dynamically consistent circulation regimes.

- **Purpose**: This classification enables aggregation of EPEs according to their governing large-scale atmospheric conditions, reducing sensitivity to individual-event variability and allowing a regime-based analysis of precipitation responses.

S5. Statistical Analysis

Paired t-test (grid-pointwise). At each grid point (i, j), let x_k and y_k denote the daily precipitation values (or other field) from the Present and Past experiments, respectively, on day k ($k = 1, \ldots, N$), where N is the total number of days in the analysis period (January 2017 – October 2024, $N = 2861$).

Define the paired differences

$$d_k = x_k - y_k, \qquad k = 1, \ldots, N,$$

with sample mean and standard deviation

$$\bar{d} = \frac{1}{N}\sum_{k=1}^{N} d_k, \qquad s_d = \sqrt{\frac{1}{N-1}\sum_{k=1}^{N}(d_k - \bar{d})^2}.$$

The t-statistic

$$t = \frac{\bar{d}}{s_d/\sqrt{N}}$$

follows a Student's t distribution with $N - 1$ degrees of freedom under the null hypothesis $H_0\colon \bar{d} = 0$, assuming the differences are independent and approximately Gaussian. The latter assumption is reasonable for large N by the central limit theorem. Two-sided p-values are computed in the standard way.

The paired t-test is an appropriate choice when analyzing daily values because the Present and Past experiments share identical large-scale circulation (spectral nudging toward ERA5), so data from the same calendar day form natural pairs.

Binomial (sign) test (annual aggregates) To assess robustness across individual years independently of the daily variance structure, we apply a non-parametric sign test on annual aggregates. For each grid point and each of the $n = 7$ complete simulation years, we record whether the annual-mean (or seasonal-mean) precipitation (or other field) in the Present experiment exceeds that in the Past experiment. Let X denote the number of years satisfying this condition. Under the null hypothesis of no systematic difference ($H_0 : p = 0.5$), X follows a binomial distribution: $X \sim \mathrm{Binom}(n = 7, 0.5)$. The two-sided p-value is computed as

$$p = 2 \min\Big\{P(X \leq x),\ P(X \geq x)\Big\}.$$

We adopt $X \geq 6$ as the significance criterion, corresponding to a two-sided p-value of $p \approx 0.063$. Although this marginally exceeds the conventional $\alpha = 0.05$ threshold, it represents the most stringent achievable criterion given the limited number of available years ($n = 7$), and is reported transparently alongside the t-test results.

S6. Evaluation of Destination Earth simulation over the Italian domain

The *Present* climate simulation of the IFS-FESOM Destination Earth model was validated against two independent reference datasets: the CERRA regional reanalysis and the ArCIS observational dataset. As shown in Figure S1, IFS-FESOM successfully reproduces the spatial patterns of key precipitation metrics over the Italian domain, despite modest systematic biases discussed below.

To further characterise these biases, Figure S2 shows pairwise differences between IFS-FESOM, CERRA, and ArCIS for the same three metrics shown in Figure S1: number of wet days, annual mean precipitation, and mean annual maxima, all evaluated over the common period 2017–2023. The right column of Figure S2 (CERRA minus ArCIS) provides an estimate of the inter-benchmark uncertainty, against which the model biases need to be interpreted.

Wet days. IFS-FESOM simulates fewer wet days than CERRA across most of the Italian domain (Figure S2a), indicating a slight dry bias relative to the reanalysis. In contrast, IFS-FESOM shows more wet days than ArCIS (panel b), consistent with the well-known tendency of high-resolution model simulations to overestimate precipitation occurrence relative to station-interpolated observational products. Importantly, CERRA itself is wetter than ArCIS (panel c). The magnitude of the CERRA–ArCIS discrepancy is comparable to or larger than the IFS-FESOM–ArCIS discrepancy, indicating that the model biases are within observational uncertainty and can not be confidently assessed.

Annual mean precipitation. A qualitatively similar picture emerges for annual mean precipitation (panels d–f): IFS-FESOM lies between the two reference datasets in most regions, and inter-benchmark differences are generally of comparable magnitude to the model biases.

Mean annual maxima. For extreme precipitation (panels g–i), IFS-FESOM exhibits a wet bias along the Tyrrhenian coast relative to CERRA (panel g), while showing an overall dry bias relative to ArCIS (panel h). Notably, CERRA itself has a dry bias relative to ArCIS for annual maxima (panel i).

Seasonal breakdown. The same bias analysis was repeated for each meteorological season (DJF, MAM, JJA, SON; not shown). The results are qualitatively consistent across all seasons, with no season exhibiting systematic biases of a sign or magnitude that would suggest a directional distortion of the thermodynamic responses analysed in this study (not shown).

Overall, across all metrics and seasons, the biases of IFS-FESOM relative to either benchmark are generally of similar magnitude to the discrepancies between the benchmarks themselves. This indicates that the uncertainty inherent in the reference datasets is comparable to the model error, and supports the conclusion that IFS-FESOM provides a realistic representation of the Italian precipitation climatology. Furthermore, since both the *Present* and *Past* simulations share the same model formulation, any systematic biases affect both experiments equally and therefore do not compromise the interpretation of their difference as a thermodynamic response to anthropogenic warming.

S7: Atmospheric stability diagnostics and seasonal contrast

MSE-based buoyancy framework. As direct CAPE and CIN diagnostics are unavailable in the DestinE simulations, parcel buoyancy is estimated following Randall (2015) from the difference between the moist static energy (MSE) of an ascending saturated parcel and that of the environment. This methodology has been widely adopted in studies of convective instability (e.g., Cook and Seager, 2013; Pascale et al., 2017; Li and Tamarin-Brodsky, 2026). The buoyancy of a saturated ascending air parcel, measured by the temperature difference between the parcel and its environment, is proportional to the difference between the environmental saturation moist static energy (MSE^*) and the MSE of the ascending saturated parcel, which is conserved during ascent since the parcel is assumed to ascend adiabatically from near the surface. Therefore, the parcel MSE can be approximated by the near-surface MSE (Randall, 2015), yielding:

$$c_p(T_{parcel} - T) \approx \frac{MSE_{\mathrm{ns}} - MSE^*}{1+\gamma}, \tag{2}$$

where $MSE = c_pT + gz + Lq$, the subscript "ns" denotes 2 m above the surface, q is the specific humidity, g is the gravitational acceleration, $c_p = 1004\ \mathrm{J\,K^{-1}\,kg^{-1}}$ is the isobaric specific heat constant of dry air, $L = 2.5 \times 10^6\ \mathrm{J\,kg^{-1}}$ is the latent heat of condensation, the asterisk denotes saturation (e.g., $q^*(T, p)$), and $\gamma = (L/c_p)(\partial q^*/\partial T)_p$. The parameter $\gamma = O(1)$ (Randall, 2015), hence $MSE_{ns} - MSE^*$ is roughly twice the buoyancy value. To assess changes in the atmospheric convective instability, we thus estimate the buoyancy index

$$B = MSE_{ns} - MSE^* \tag{3}$$

above the lifting condensation level (LCL). We refer to the quantity evaluated at 500 hPa as the *Mid-Tropospheric Buoyancy* and at 700 hPa as the *Lower-Tropospheric Buoyancy*. Finally we estimate $\Delta B = \Delta(MSE_{ns} - MSE^{*})$, where the difference Δ is taken between the Present and Past runs (Fig. S3), and negative (positive) values of B indicate downward (upward) acceleration. Such differences, evaluated at 500 and 700 hPa are informative, respectively, of changes in CAPE and CIN.

To isolate regimes analogous to CAPE and CIN, we apply selective retention of values by sign. At 500 hPa, only positive values of B are retained — timesteps at which the surface parcel is buoyant relative to the mid-troposphere — as a proxy for CAPE, indicating an unstable deep-tropospheric column. At 700 hPa, only negative values are retained — timesteps at which the parcel is inhibited below 700 hPa — as a proxy for CIN, indicating a stable lower-tropospheric cap. Changes in Mid-Tropospheric Buoyancy (CAPE proxy) and Lower-Tropospheric Buoyancy (CIN proxy) between the Present and Past experiments therefore diagnose how warming modifies the convective environment, even in the absence of full CAPE/CIN output.

The results presented in Fig. S3 were computed at 15 UTC, corresponding to the typical onset time of summer convection over the Italian domain. Similar results are obtained when the analysis is performed at 13 UTC (not shown), indicating that the findings are robust to the choice of analysis time.

JJA: land–ocean warming contrast and suppressed convective initiation. During JJA, land surfaces over Italy warm faster than the surrounding sea (mean $\Delta T_{\mathrm{land}} =$ 2.3 °C versus mean $\Delta T_{\mathrm{SST}} = 1.8$ °C; Fig. S4), thereby enhancing the land–sea thermal contrast. As a result, near-surface relative humidity decreases (Fig. S3a), because continental specific humidity does not increase sufficiently to compensate for the rise in saturation vapour pressure over the warmer land surface, owing to limited moisture availability. The resulting decrease in relative humidity raises the LCL (not shown), as air parcels must ascend farther and cool more before reaching saturation. Because the level of free convection (LFC) cannot occur below the lifting condensation level (LCL), convective parcels must rise to greater heights before attaining positive buoyancy. This increases the energetic barrier to deep convection and reduces the likelihood of convective initiation.

The near-surface moisture deficit further stabilizes the lower troposphere by reducing MSE_{ns} relative to MSE^{*}_{700}. Consistent with this mechanism, the Lower-Tropospheric Buoyancy decreases (Fig. S3c), i.e. becomes more negative, indicating stronger inhibition of ascending parcels and thus a larger CIN analogue.

At the same time, the Mid-Tropospheric Buoyancy increases (Fig. S3b). Although lower-tropospheric stability strengthens, near-surface warming and moistening increase MSE_{ns} more rapidly than warming aloft increases MSE^{*}_{500}. Consequently, the parcel–environment MSE contrast above the LFC becomes larger, enhancing parcel buoyancy and increasing the CAPE analogue. This behaviour is consistent with the typical response of summertime continental convection to climate warming: over land, near-surface warming generally exceeds that aloft owing to the limited heat capacity of the land surface and, in many regions, reduced soil-moisture availability (e.g., Seeley and Romps, 2015; Chen et al., 2020). As a result, boundary-layer MSE increases more rapidly than the saturation MSE of the free troposphere, favouring larger CAPE despite the concurrent increase in convective inhibition.

The combination of increased lower-tropospheric stability and increased mid-tropospheric instability thus provides a physically consistent explanation for the observed changes. The more stable lower troposphere suppresses convective initiation, reducing the occurrence of light-to-moderate precipitation events, consistent with the decrease in wet days. When initiation is eventually triggered by sufficiently strong forcing, the larger available CAPE produces more intense events, consistent with the increase in mean seasonal precipitation maxima. This increased-CIN/increased-CAPE regime under warming thus simultaneously accounts for both signals – reduction in wet days and increase in mean seasonal maxima-, without requiring any change in the large-scale circulation, which is held fixed by construction in the nudged simulations.

SON: unrestricted CAPE increase and enhanced extreme intensification. The response of seasonal atmospheric stability differs between SON and JJA. In JJA, the Lower-Tropospheric Buoyancy decreases while the Mid-Tropospheric Buoyancy increases under warming, indicating simultaneously stronger convective inhibition and larger potential energy available when initiation is achieved. In SON, by contrast, the Mid-Tropospheric Buoyancy increases across the whole domain (Fig. S3e), indicating greater CAPE available for deep convection, while the Lower-Tropospheric Buoyancy remains broadly unchanged or increases slightly over northern Italy (Fig. S3f), meaning convective initiation is not suppressed as in JJA. The absence of increased CIN in SON thus allows the larger available CAPE to be realised more frequently, contributing to a stronger and more spatially uniform intensification of extreme precipitation.

S8. WT Composites: Top-Three vs. All-Events

Two complementary composite strategies are employed in this study to characterise the thermodynamic response of extreme precipitation to AGW within each weather type (WT).

Top-three composites. For each warning area (WA) and each WT, the three most intense extreme precipitation events (EPEs) are selected. The composites are then computed as the average across these three events. This approach is designed to sharpen the spatial representation of the warming signal for the most severe extremes: when compositing over all EPEs associated with a given WT, the spatial variability of individual events, their limited spatial extent, and their differing centres of action tend to smooth and dilute the local signal. By retaining only the three most intense events at each grid point, this approach provides information on extremes. Because of this limited sample size, formal significance testing cannot be applied to the top-three composites.

All-events composites. The all-events composites are constructed by averaging over all EPEs assigned to a given WT, regardless of intensity. The number of EPEs per WT ranges from 34 to 81 over the 2017–2023 period, providing a sample size sufficient for paired t-test significance assessment. While the all-events composites capture the mean thermodynamic response across the full range of events associated with each WT, they are not directly informative of changes in local extremes, since the events within each composite will tend to occur at different locations.

Consistency between the two approaches. Figure S7 shows the all-events composites for each WT alongside their climate-change response. The spatial patterns are broadly consistent with those from the top-three composites presented in the main text (Figure 4), with statistically significant responses emerging in the same regions. Taken together, the two compositing strategies provide complementary perspectives – the all-events composites establish the statistical significance of the mean WT response, while the top-three composites highlight where the most severe extremes are preferentially intensified under warming.

Supplementary figures

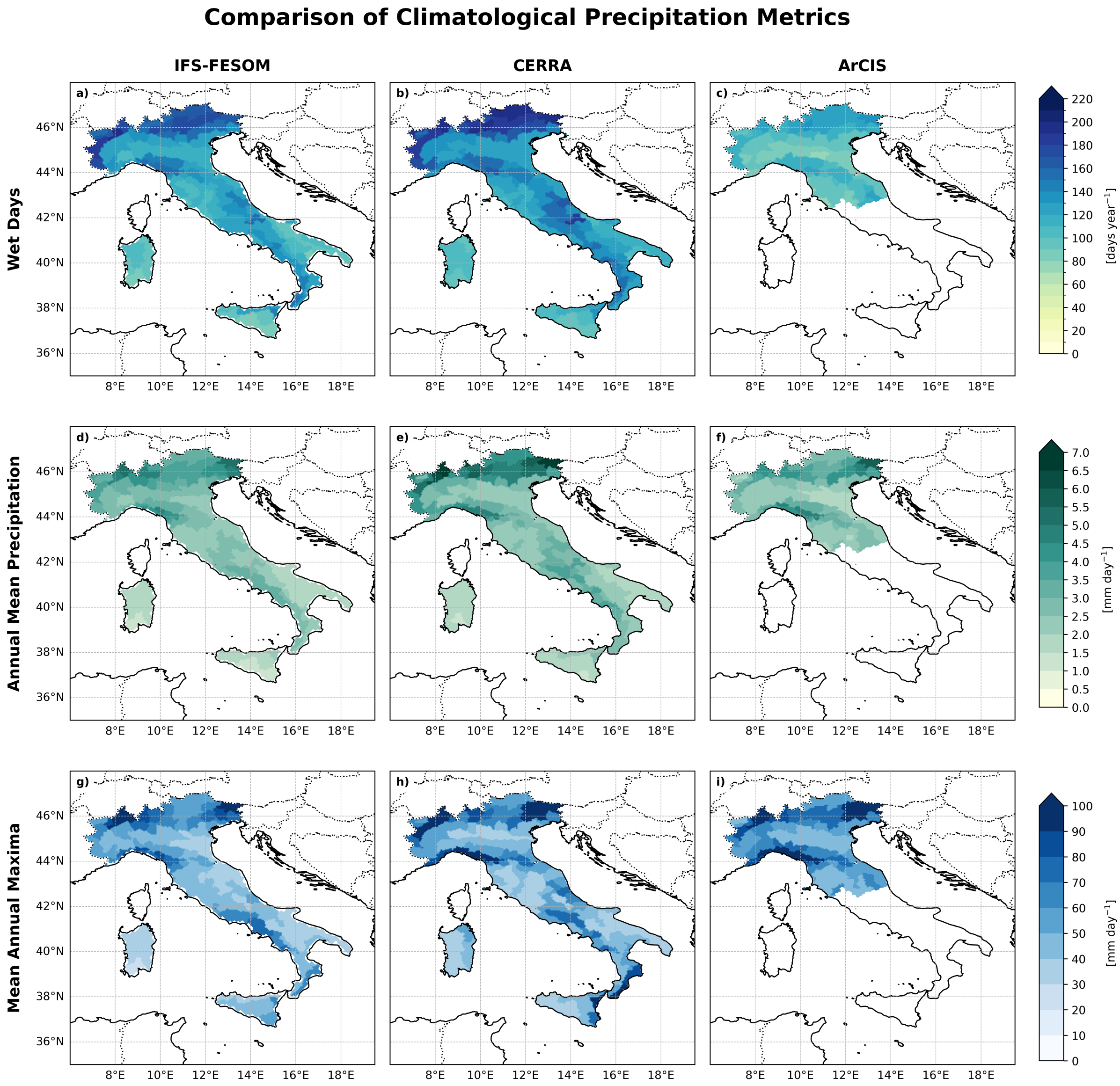

Figure S1: Evaluation of IFS-FESOM precipitation over Italy. (a) number of wet days [days year^{-1}] in IFS-FESOM, (b) CERRA, and (c) ArCIS. (d-f) as in (a-c) but for the annual mean precipitation [mm day^{-1}]. (g-i) as in (a-c) but for the mean annual maxima [mm day^{-1}]. All three datasets (IFS-FESOM, CERRA, ArCIS) were analysed over the common period 2017-2023.

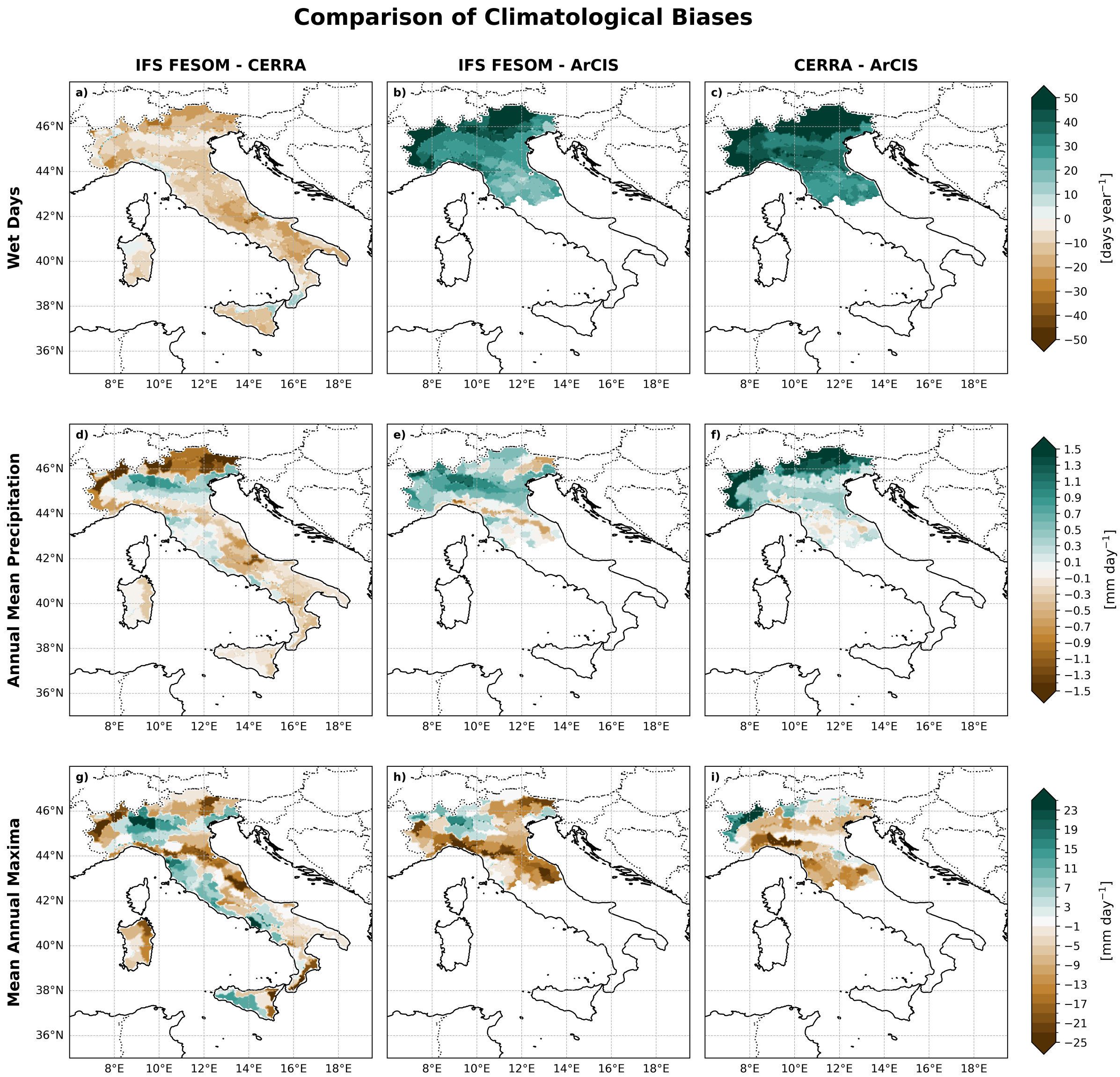

Figure S2: Evaluation of IFS-FESOM *Present* simulation precipitation biases over Italy for the period 2017–2023 against the reference datasets ArCIS and CERRA. Panels (a–c) show biases in the annual number of wet days [days year^{-1}], (d–f) biases in annual mean precipitation [mm day^{-1}], and (g-i) biases in mean annual maxima [mm day^{-1}]. In each row, the left, centre, and right columns display IFS-FESOM minus CERRA, IFS-FESOM minus ArCIS, and CERRA minus ArCIS, respectively. The latter provides an estimate of the observational/reanalysis uncertainty against which model biases should be interpreted. All datasets were analysed over the common period 2017–2023 and regridded onto a common grid prior to comparison.

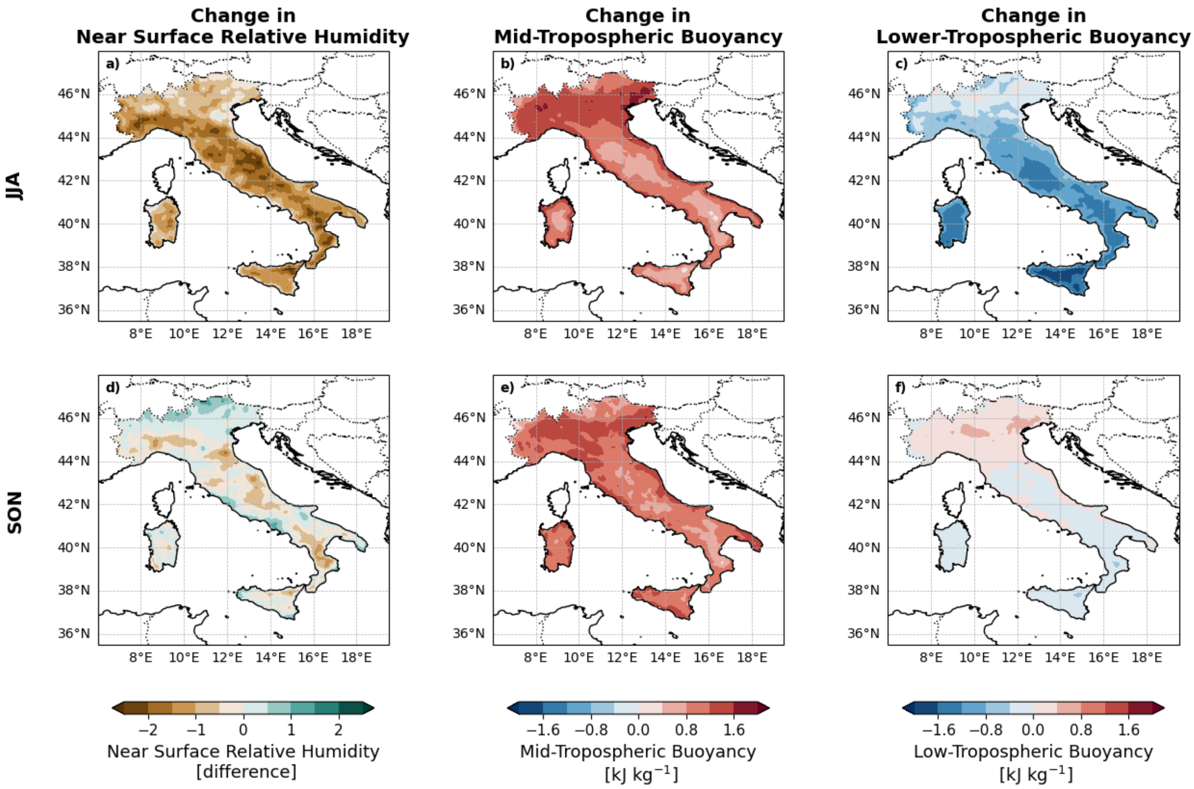

Figure S3: Comparison of atmospheric stability indicators between the Present and Past simulations of the IFS-FESOM Destination Earth Climate Digital Twin. Change in mean JJA (a) near-surface relative humidity (%), (b) mid-tropospheric buoyancy at 500 hPa, (c) lower-tropospheric buoyancy at 700 hPa. (d-f) as in (a-c) but for SON. For mid-tropospheric and lower-tropospheric buoyancy, the changes are computed retaining only the days with positive and negative buoyancy, respectively. See Section S8 for more details.

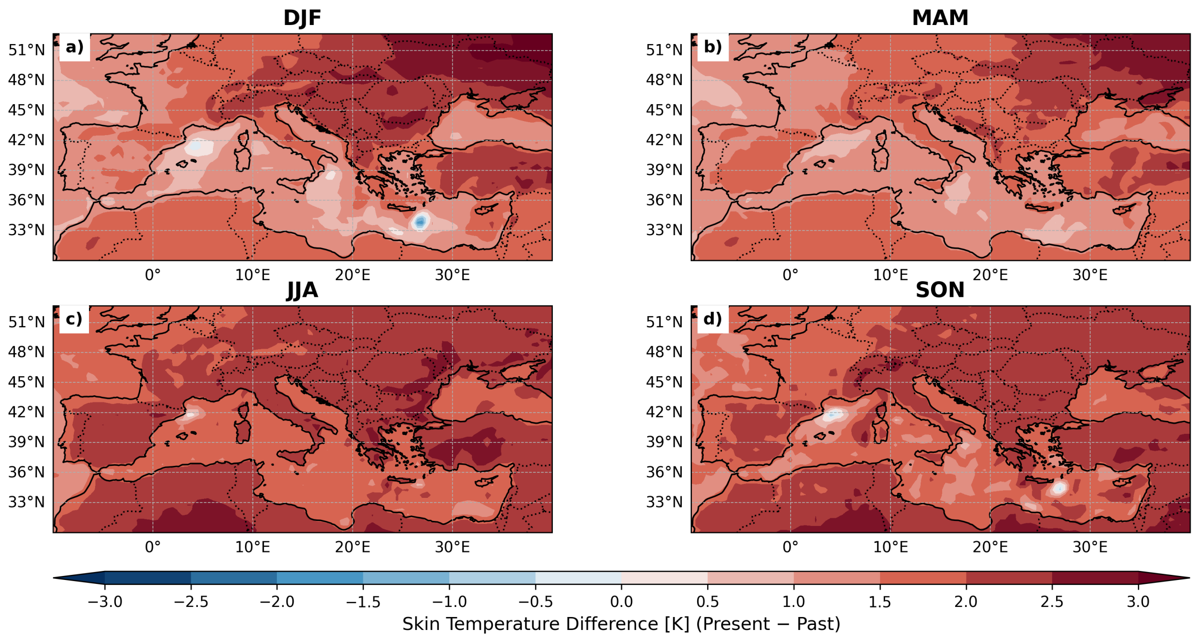

Figure S4: Seasonal skin temperature difference between the Present and Past (1950s) climate simulations of the IFS-FESOM Destination Earth Climate Digital Twin for Adaptation.

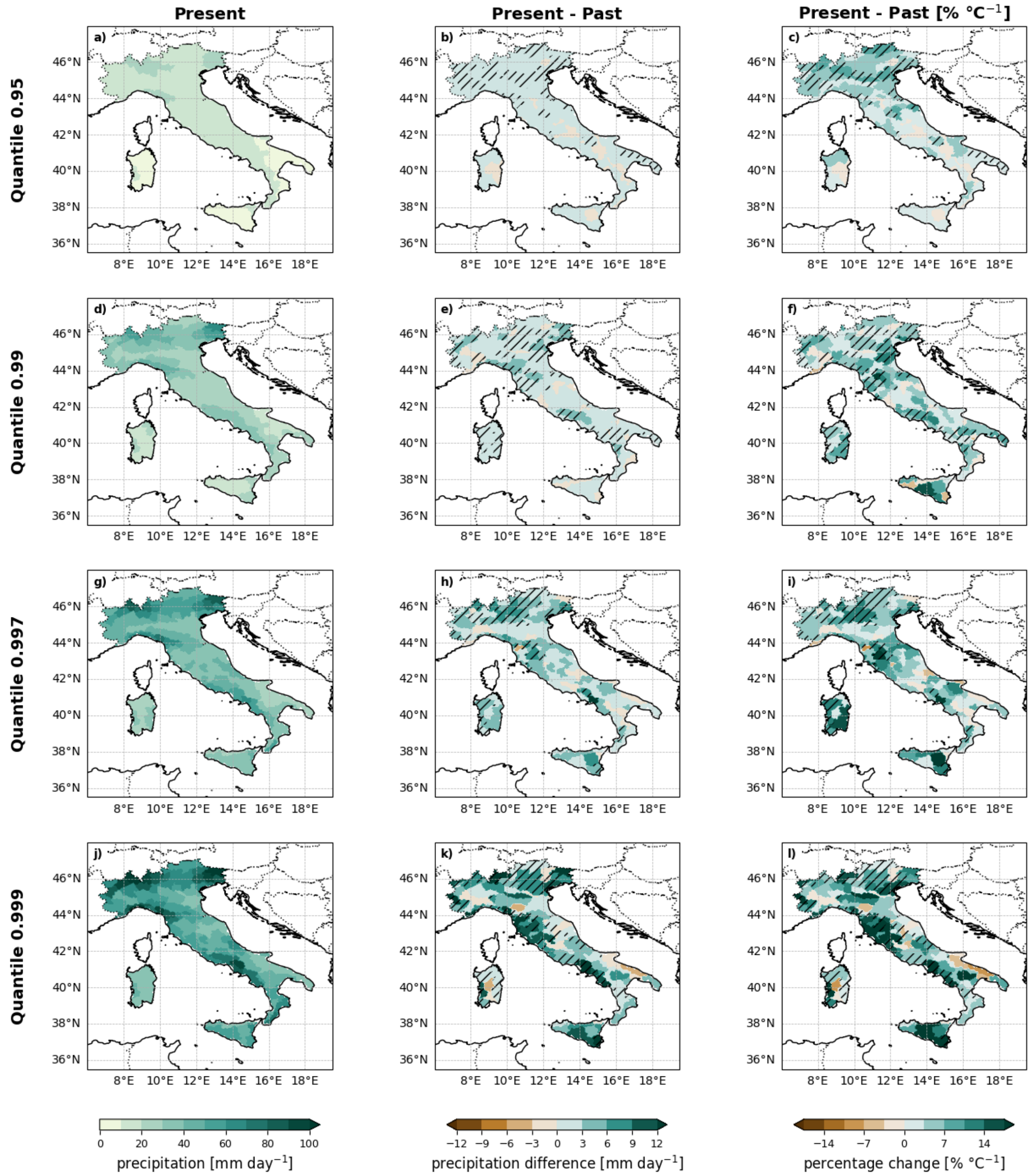
Present
Present - Past
Present - Past [% °C^{-1}]
Quantile 0.95
Quantile 0.99
Quantile 0.997
Quantile 0.999
a)
b)
c)
d)
e)
f)
g)
h)
i)
j)
k)
l)
46°N
44°N
42°N
40°N
38°N
36°N
8°E
10°E
12°E
14°E
16°E
18°E
0 20 40 60 80 100
precipitation [mm day^{-1}]
−12 −9 −6 −3 0 3 6 9 12
precipitation difference [mm day^{-1}]
−14 −7 0 7 14
percentage change [% °C^{-1}]

Figure S5: [Previous Page] Comparison of precipitation quantiles between the Present and Past (1950s) IFS–FESOM Destination Earth Climate Digital Twin for Adaptation simulations. Panels (a,d,g,j) show the quantile fields in the Present simulation, panels (b,e,h,k) show the absolute difference between the Present and Past simulations, and panels (c,f,i,l) show the corresponding response expressed in % $°C^{-1}$ (difference normalized by the Past values and by the global mean surface temperature difference between the two simulations, $\Delta GMST = 1.23$ K). Each row corresponds to a different precipitation quantile level. Hatched regions indicate areas where the response is statistically significant at the 5% level based on a paired binomial test.

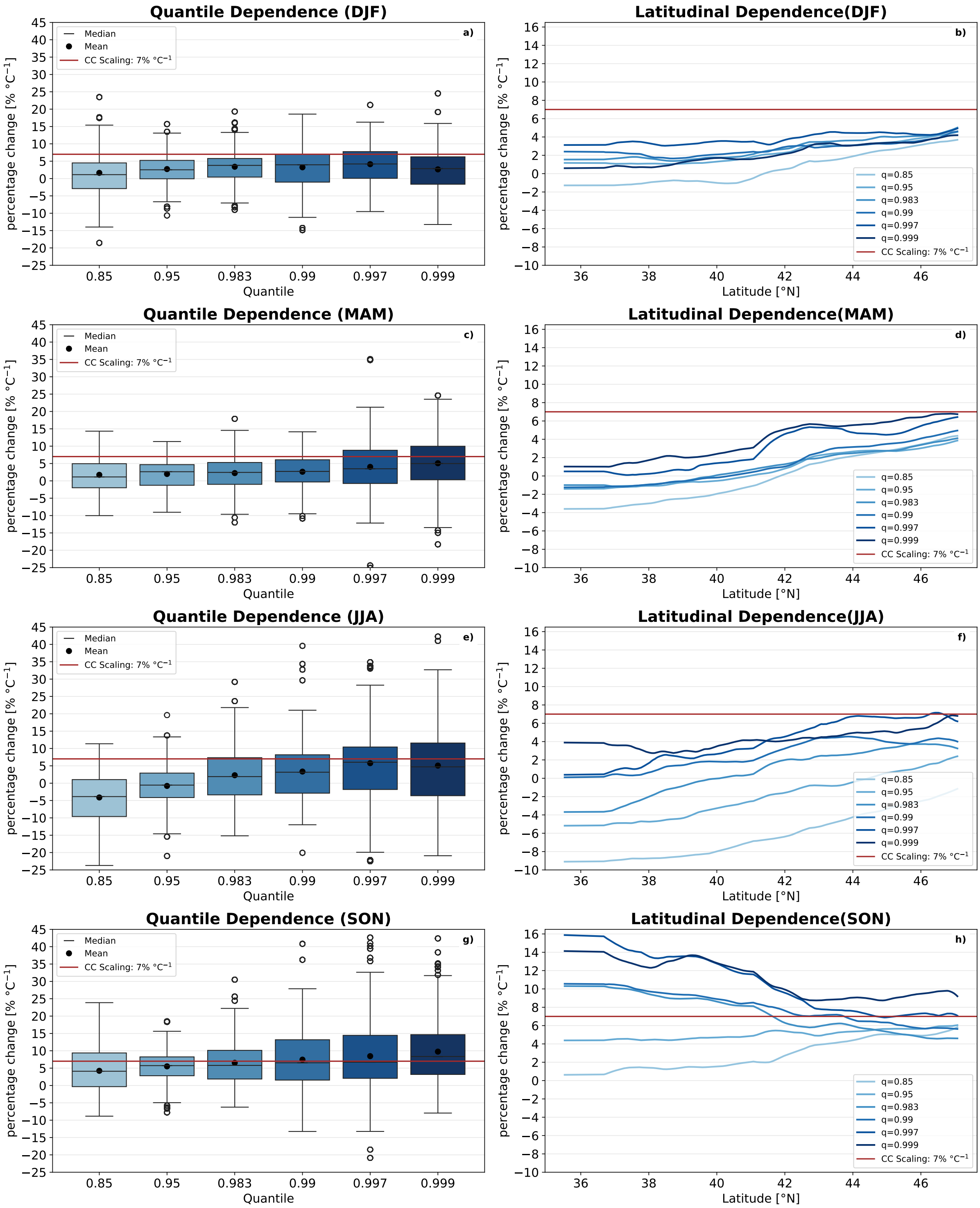
Quantile Dependence (DJF)
a)
Latitudinal Dependence(DJF)
b)
Quantile Dependence (MAM)
c)
Latitudinal Dependence(MAM)
d)
Quantile Dependence (JJA)
e)
Latitudinal Dependence(JJA)
f)
Quantile Dependence (SON)
g)
Latitudinal Dependence(SON)
h)
Median
Mean
CC Scaling: 7% °C⁻¹
q=0.85
q=0.95
q=0.983
q=0.99
q=0.997
q=0.999
percentage change [% °C⁻¹]
Quantile
Latitude [°N]

Figure S6: [Previous Page] Seasonal dependence of precipitation changes across quantiles and latitude. (a,c,e,g) Box plots of percentage change per degree of warming (% $°C^{-1}$) across quantiles, computed from all grid points over Italy. For each quantile, values are aggregated domain-wide; the central line shows the median, the dot the mean, boxes the interquartile range (IQR), and whiskers extend to 1.5 IQR. Outliers denote regions with strong local deviations. (b,d,f,h) Latitudinal profiles for the same quantiles, obtained via longitudinal averaging and a centered 5° rolling mean. The red line indicates the Clausius–Clapeyron (7 % $°C^{-1}$) scaling.

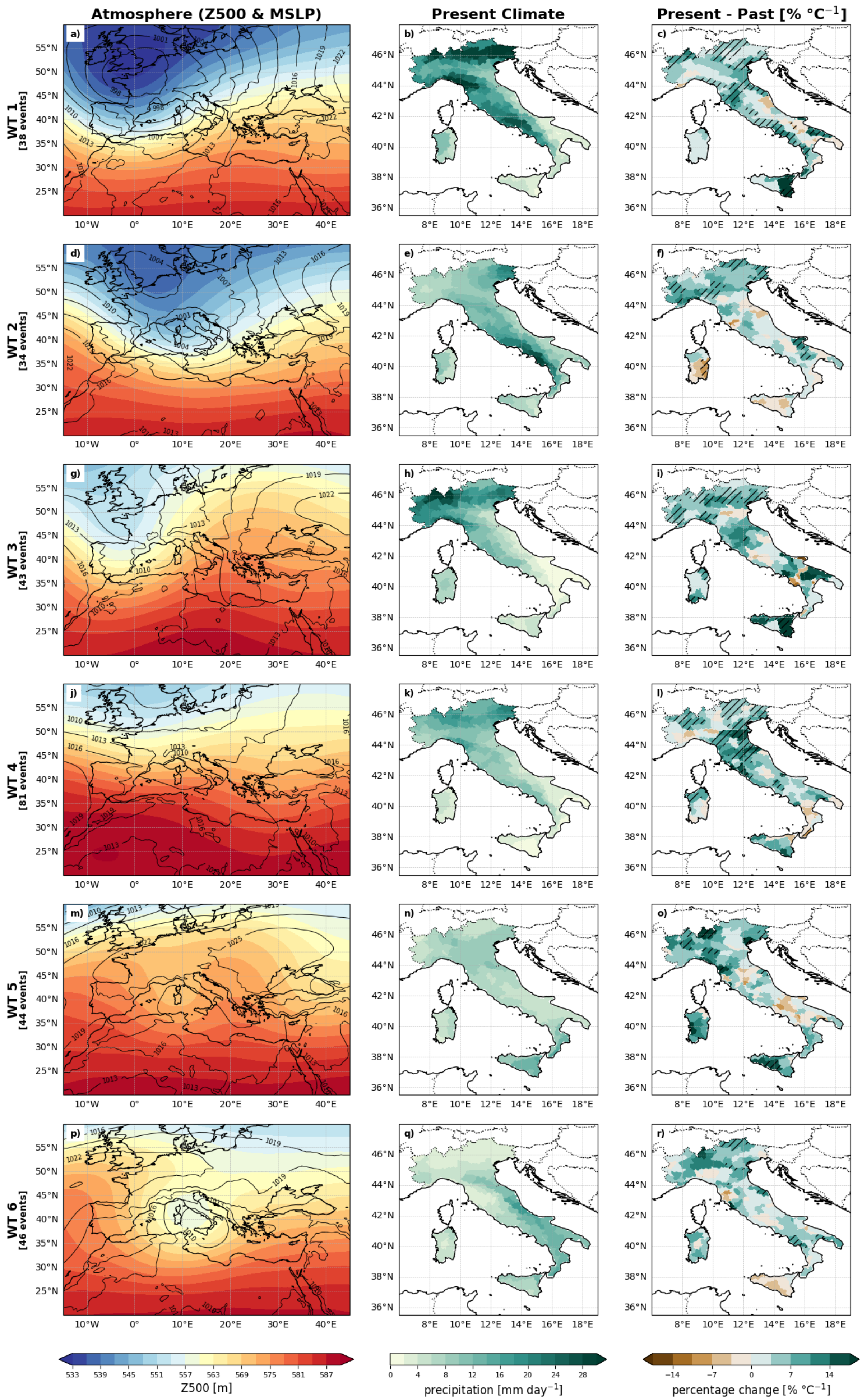
Atmosphere (Z500 & MSLP)
Present Climate
Present - Past [% °C^{-1}]
WT 1 [38 events]
WT 2 [34 events]
WT 3 [43 events]
WT 4 [81 events]
WT 5 [44 events]
WT 6 [46 events]
Z500 [m]
precipitation [mm day^{-1}]
percentage change [% °C^{-1}]

Figure S7: [Previous Page] Response of precipitation across Weather Types associated with Italian precipitation extremes. Panels (a–c) show WT1: (a) Present-climate mean sea-level pressure (MSLP; contours) and 500 hPa geopotential height (Z500; shading), (b) Present-climate composite precipitation based on all extreme events per warning area, and (c) the climate-change response (% $°C^{-1}$), computed as the Present–Past (1950s) difference normalized by Past precipitation and by the global-mean surface temperature difference (ΔGMST = 1.23 °C). Panels (d–f), (g–i), (j–l), (m–o), and (p–r) show WT2–WT6 with the same layout. The number of EPEs used for each composite is indicated below the WT label. Hatched regions are statistically significant at the 5% level based on a paired t-test.

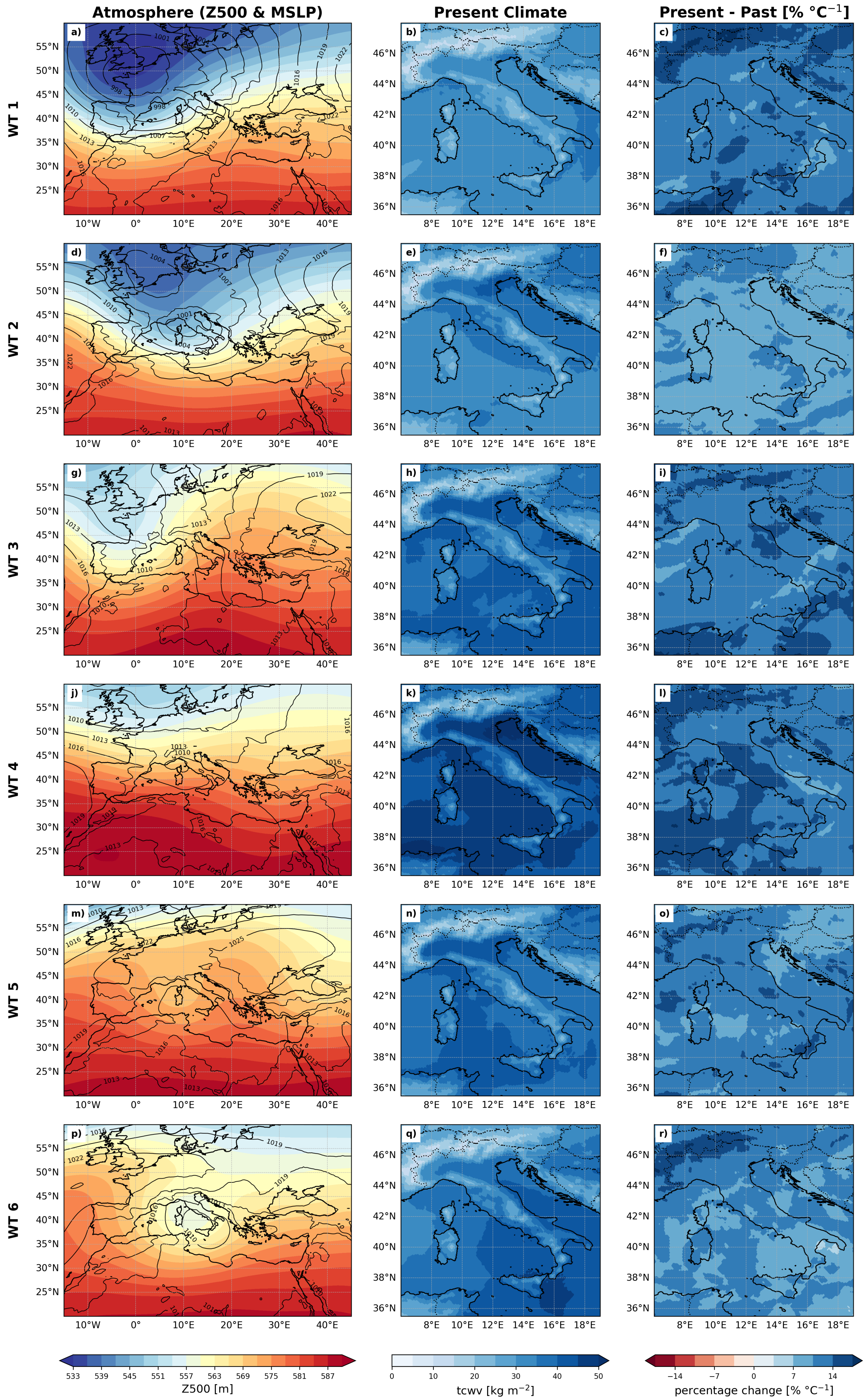
Atmosphere (Z500 & MSLP)
Present Climate
Present - Past [% °C^{-1}]
WT 1
WT 2
WT 3
WT 4
WT 5
WT 6
a)
b)
c)
d)
e)
f)
g)
h)
i)
j)
k)
l)
m)
n)
o)
p)
q)
r)
55°N
50°N
45°N
40°N
35°N
30°N
25°N
10°W
0°
10°E
20°E
30°E
40°E
46°N
44°N
42°N
40°N
38°N
36°N
8°E
10°E
12°E
14°E
16°E
18°E
533 539 545 551 557 563 569 575 581 587
Z500 [m]
0 10 20 30 40 50
tcwv [kg m^{-2}]
−14 −7 0 7 14
percentage change [% °C^{-1}]

Figure S8: [Previous Page] Response of total column water vapor (TCWV) across atmospheric weather types (WTs) over Italy. Panels (a–c) show WT1: (a) present-climate composite from the top three extreme events per warning area, (b) Present–Past (1950s) difference, and (c) climate-change response in % $°C^{-1}$, normalized by the global mean surface temperature difference (ΔGMST = 1.23 °C). Panels (d–f), (g–i), (j–l), (m–o), and (p–r) show the same for WT2–WT6, respectively.

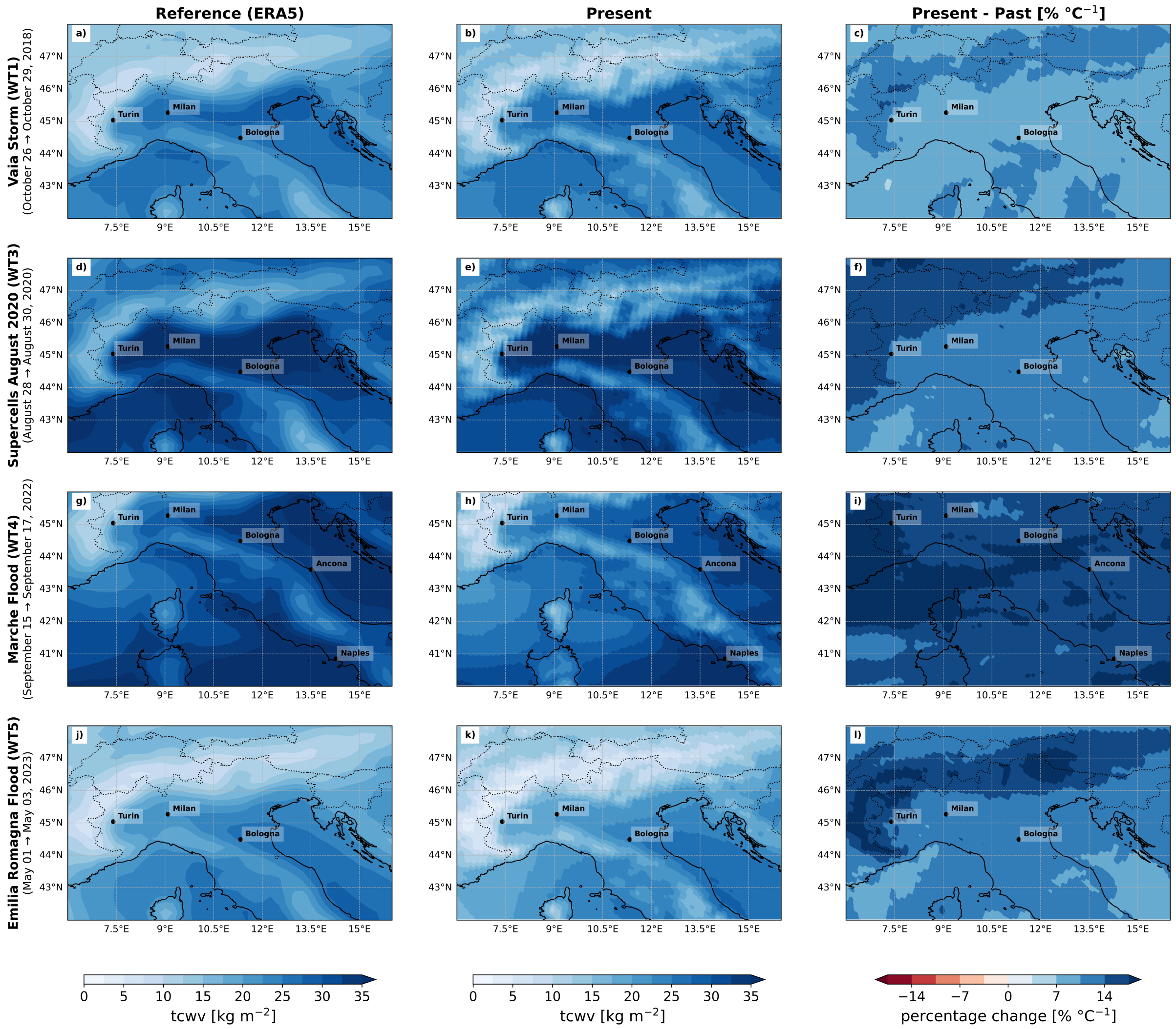

Figure S9: Total column water vapor (TCWV) fields for the four extreme precipitation case studies over Italy discussed in the main text. Panels (a,d,g,j) show the events in the ERA5 observational dataset, used as reference. Panels (b,e,h,k) show the corresponding events in the Present-climate simulation of the IFS–FESOM Destination Earth Climate Digital Twin for Adaptation. Panels (c,f,i,l) show the climate-change response for each event, calculated as the difference between Present and Past (1950s) simulations, normalized by the Past TCWV and by the global mean surface temperature difference between the two simulations (ΔGMST = 1.23 °C), and expressed in % °C^{-1}. Each row corresponds to one event; the event name and the accumulation period over which TCWV has been computed are indicated in the panels.

References

J. Chen, A. Dai, Y. Zhang, and K. L. Rasmussen. Changes in convective available potential energy and convective inhibition under global warming. *Journal of Climate*, 33:2025–2050, 2020. doi: 10.1175/JCLI-D-19-0461.1.

B. I. Cook and R. Seager. The response of the North American Monsoon to increased greenhouse gas forcing. *Journal of Geophysical Research: Atmospheres*, 118:1690–1699, 2013. doi: 10.1002/jgrd.50111.

S. Danilov, D. Sidorenko, Q. Wang, and T. Jung. The Finite-volumE Sea ice–Ocean Model (FESOM2). *Geoscientific Model Development*, 10:765–789, 2017. doi: 10.5194/gmd-10-765-2017.

M. Diamantakis and F. Váňa. A fast converging and concise algorithm for computing the departure points in semi-Lagrangian weather and climate models. *Quarterly Journal of the Royal Meteorological Society*, 148:670–684, 2022. doi: 10.1002/qj.4224.

M. Hortal. The development and testing of a new two-time-level semi-Lagrangian scheme (SETTLS) in the ECMWF forecast model. *Quarterly Journal of the Royal Meteorological Society*, 128:1671–1687, 2002. doi: 10.1002/qj.200212858314.

C. Iacomino, S. Pascale, G. Zappa, M. Iotti, F. Grazzini, P. Ghinassi, and A. Portal. A Classification of High-Risk Atmospheric Circulation Patterns for Italian Precipitation Extremes. *International Journal of Climatology*, 45:e70118, 2025. doi: 10.1002/joc.70118.

A. John, S. Beyer, M. Athanase, A. Sánchez-Benítez, H. F. Goessling, A. Hossain, R. Aguridan, M. Andrés-Martínez, A. Gaya-Àvila, S. K. Cheedela, P. Geier, R. Ghosh, I. Hadade, N. Koldunov, S. Milinski, M. Nurisso, X. Pedruzo-Bagazgoitia, T. Rackow, I. Sandu, D. Sidorenko, J. Streffing, E. Vitali, and T. Jung. Global Kilometer-Scale Climate Storylines Using Spectral Nudging. *Journal of Advances in Modeling Earth Systems*, 18:e2025MS005326, 2026. doi: 10.1029/2025MS005326.

F. Li and T. Tamarin-Brodsky. Atmospheric stability sets maximum moist heat and convection in the midlatitudes. *Science Advances*, 12:eaea8453, 2026. doi: 10.1126/sciadv.aea8453.

S. Pascale, W. R. Boos, S. Bordoni, T. L. Delworth, S. B. Kapnick, H. Murakami, G. A. Vecchi, and W. Zhang. Weakening of the North American monsoon with global warming. *Nature Climate Change*, 7:806–812, 2017. doi: 10.1038/nclimate3412.

D. Randall. *An Introduction to the Global Circulation of the Atmosphere | Princeton University Press*. 2015. ISBN: 9780691148960.

P. Scholz, D. Sidorenko, O. Gurses, S. Danilov, N. Koldunov, Q. Wang, D. Sein, M. Smolentseva, N. Rakowsky, and T. Jung. Assessment of the Finite-volumE Sea ice-Ocean Model (FESOM2.0) – Part 1: Description of selected key model elements and comparison to its predecessor version. *Geoscientific Model Development*, 12:4875–4899, 2019. doi: 10.5194/gmd-12-4875-2019.

P. Scholz, D. Sidorenko, S. Danilov, Q. Wang, N. Koldunov, D. Sein, and T. Jung. Assessment of the Finite-VolumE Sea ice–Ocean Model (FESOM2.0) – Part 2: Partial bottom cells, embedded sea ice and vertical mixing library CVMix. *Geoscientific Model Development*, 15:335–363, 2022. doi: 10.5194/gmd-15-335-2022.

J. T. Seeley and D. M. Romps. Why does tropical convective available potential energy (cape) increase with warming? *Geophysical Research Letters*, 42:10429–10437, 2015. doi: 10.1002/2015GL066199.

C. Temperton, M. Hortal, and A. Simmons. A two-time-level semi-Lagrangian global spectral model. *Quarterly Journal of the Royal Meteorological Society*, 127:111–127, 2001. doi: 10.1002/qj.49712757107.